Research Square

Preprints are preliminary reports that have not undergone peer review.
They should not be considered conclusive, used to inform clinical practice,
or referenced by the media as validated information.

Quantitative Texture Analysis of Trabecular Bone Alterations Surrounding Vertical Root Fractures on Panoramic Radiographs

Kyuseok Kim
Gachon University
Sung-Min Hwang
Kyungpook National University
Youngjin Lee
Gachon University
Young-Eun Kwon
yekwon@knu.ac.kr

Kyungpook National University

Research Article

Keywords: Tooth Fractures, Radiography, Panoramic, Diagnostic Imaging, Image Processing, Computer-Assisted

Posted Date: April 1st, 2026

DOI: https://doi.org/10.21203/rs.3.rs-9174810/v1

License: This work is licensed under a Creative Commons Attribution 4.0 International License.
Read Full License

Additional Declarations: No competing interests reported.

Quantitative Texture Analysis of Trabecular Bone Alterations Surrounding Vertical Root Fractures on Panoramic Radiographs

Kyuseok Kim[1†], Sung-Min Hwang[2†], Youngjin Lee[3*], Young-Eun Kwon[4*]

[1]Institute of Human Convergence Health Science, Gachon University, Incheon, Republic of Korea

[2]Department of Periodontology, School of Dentistry, IHBR, Kyungpook National University, Daegu, Republic of Korea

[3] Department of Radiological Science, Gachon University, Incheon, Republic of Korea

[4] Department of Oral and Maxillofacial Radiology, School of Dentistry, IHBR, Kyungpook National University, Daegu, Republic of Korea

[†]These authors contributed equally to this work

[*]Correspondence to Prof. Youngjin Lee & Young-Eun Kwon

***Youngjin Lee, PhD**

Department of Radiological Science, Gachon University, Republic of Korea

E-mail: yj20@gachon.ac.kr

*** Young-Eun Kwon, DDS, PhD**

Department of Oral and Maxillofacial Radiology, School of Dentistry, IHBR, Kyungpook National University, Republic of Korea

E-mail : yekwon@knu.ac.kr

ORCID

Kyuseok Kim: 0000-0002-7627-7394

Sung-Min Hwang: 0000-0002-2701-4854

Youngjin Lee: 0000-0002-6848-7666

Young-Eun Kwon: 0000-0001-5795-6968

Acknowledgements

Not applicable.

Funding

This work was supported by Kyungpook National University Dental Hospital Institute for Dental Research (2025)

Quantitative Texture Analysis of Trabecular Bone Alterations Surrounding Vertical Root Fractures on Panoramic Radiographs

Objectives

Vertical root fractures (VRFs) are difficult to diagnose on panoramic radiographs because fracture lines are often not clearly visible. This study aimed to quantitatively evaluate trabecular bone alterations surrounding VRF roots using texture analysis of panoramic images and to identify indirect imaging features that may assist in VRF assessment.

Materials and Methods

This retrospective single-center study included 38 patients with surgically confirmed 40 VRF roots and 40 matched control roots without clinical or radiographic signs of VRF. Seven anatomically standardized Region of Interests (ROIs) were manually defined around each root. Six texture features, including gray-level co-occurrence matrix (GLCM) parameters (contrast, ASM, entropy, IDM), fractal dimension (FD), and lacunarity, were extracted. Inter-observer reliability was assessed using intraclass correlation coefficients (ICC) and Bland–Altman analysis. Group differences were evaluated using ROI-level comparisons, relative percentage change (Δ%), and inter-feature correlation analysis.

Results

Overall ROI-averaged analysis of texture features demonstrated substantial overlap between groups. However, ROI-based analysis revealed consistent directional differences. GLCM contrast decreased by approximately 11–29% across all ROIs in the VRF group, whereas IDM increased by 14–19% ($p < 0.001$). Lacunarity showed region-specific differences. Although FD did not differ significantly in absolute terms, moderate shifts in inter-feature correlations involving FD ($\Delta r = 0.20–0.30$) were observed. Inter-observer reliability demonstrated good-to-excellent agreement.

Conclusions

ROI-based quantitative texture analysis of panoramic radiographs identified spatially organized trabecular bone alterations associated with VRF, even in the absence of a clearly visible fracture line. These findings suggest that texture-based features derived from routinely acquired panoramic images may provide complementary information in VRF evaluation.

Keywords: Tooth Fractures; Radiography, Panoramic; Diagnostic Imaging; Image Processing, Computer-Assisted

Introduction

A vertical root fracture (VRF) is defined as a longitudinal fracture that extends along the long axis of the tooth root [1–4]. Structurally, it represents a disruption encompassing the cementum, dentin, and the root canal system, typically initiating from the internal root canal wall and propagating toward the outer root surface[1, 4–6]. A VRF is classified as complete or incomplete. An incomplete VRF involves only one side of the root, while a complete VRF refers to one in which the fracture plane traverses from one proximal surface to the opposite side[2, 5, 6]. VRFs are most commonly oriented in a bucco-lingual direction, while the term "split tooth" is reserved for cases where there is a visible separation of the fractured components[3–6]. While VRFs can occur in teeth with vital pulps, they are predominantly associated with endodontically treated teeth. The reported prevalence of VRFs ranges from 3.7% to 30.8%[2, 4, 7, 8]. Susceptibility is highest in the posterior region, with maxillary premolars and the mesial roots of mandibular molars most commonly affected[2, 4, 6, 8, 9]. The etiology is often iatrogenic, resulting from excessive forces during root canal condensation, over-preparation of the root canal, or the placement of intracanal posts[2, 4, 7, 8]. Additionally, repetitive masticatory forces and occlusal trauma serve as significant contributory physical factors[4, 6]. Clinically, VRFs remain difficult to diagnose because of their insidious onset and the lack of specific early symptoms[1–3, 5, 10]. As the fracture propagates, it creates a pathway for oral microorganisms into the periapical tissues, leading to periodontal destruction characterized by localized deep periodontal pockets, characteristic J-shaped or halo-shaped radiolucencies, and the development of sinus tracts[1, 4, 6, 8, 10].

Previous studies that aimed at improving the diagnosis of VRFs have primarily focused on several complementary approaches, including quantification of periapical radiolucency

patterns on intraoral radiographs, identification of epidemiologic and clinical correlates of VRF in specific patient populations, and direct detection of fracture lines on panoramic images using convolutional neural networks[4, 8, 11]. Additionally, the effectiveness of cone-beam computed tomography (CBCT) for diagnosing VRF has been extensively investigated[12]. While CBCT provides three-dimensional assessment and higher sensitivity for VRF detection, its routine use as a screening modality is limited by higher radiation exposure, increased cost, and susceptibility to beam-hardening artifacts from endodontic canal filling materials or metallic posts[6, 10, 12, 13]. More recently, AI-based CBCT approach for VRF detection have shown promising results[3].

Despite these advances, many existing diagnostic strategies continue to rely on localized lesion morphology, clinical symptom patterns, or explicit visualization of fracture lines[3, 4, 8, 11]. Panoramic radiographs are often used for VRF detection due to their availability and relatively low radiation dose. However, direct identification of fracture lines on panoramic radiographs remains inherently challenging due to limited spatial resolution, geometric distortion, and superimposition of anatomical structures[7, 11, 14]. These limitations highlight the need for alternative diagnostic paradigms that do not depend solely on direct fracture visualization. Accordingly, the present study re-evaluates panoramic radiography not as a modality for fracture line detection, but as a means to capture quantitative, region-dependent trabecular bone reorganization surrounding VRF teeth[1, 7, 14–16].

Texture analysis provides a quantitative framework for characterizing spatial patterns within medical images that are not readily appreciable through visual inspection and may reflect underlying microarchitectural alterations in bone[14,17,18]. Texture-based metrics, such as gray-level co-occurrence matrix (GLCM) features, fractal dimension (FD), and lacunarity, have

been shown to correlate with trabecular bone microarchitecture[15–22]. Moreover, these techniques can sensitively capture changes in bone complexity and spatial organization associated with systemic conditions and local pathological or treatment-related processes[13, 15–18, 23, 24]. Furthermore, these quantitative bone parameters enable the objective and reproducible assessment of trabecular architecture, and multiple studies have confirmed their utility in identifying bone alterations associated with various medical conditions and mechanical influences[13–16, 19, 20, 23].

The application of texture analysis to panoramic radiographs may offer a means to identify fracture-related trabecular bone alterations surrounding VRF teeth, even when direct fracture lines are not clearly visible. By applying objective texture descriptors to anatomically standardized region of interest (ROI), panoramic radiographs were hypothesized to contain indirect, quantifiable information reflecting fracture-associated trabecular bone reorganization. To the best of our knowledge, this is the first study to evaluate texture analysis–based trabecular bone alterations surrounding VRF teeth on panoramic radiographs. This study aimed to investigate the feasibility and diagnostic potential of texture analysis for detecting VRF on panoramic radiographs, with particular emphasis on identifying subtle trabecular bone alterations surrounding vertically fractured roots.

Materials and Methods

2.1. Study design and patient selection

This retrospective study was approved by the Institutional Review Board of Kyungpook National University Dental Hospital (IRB No. KNUDH-2025-07-05-00). Patients who visited the Department of Periodontology at Kyungpook National University Dental Hospital between 2015 and 2025, underwent panoramic radiographic examinations, showed no definitive

radiographic vertical fracture lines, but presented with clinical signs and localized alveolar bone loss suggestive of VRF were initially considered suspected VRF cases. These roots subsequently underwent periodontal surgical exploratory flap procedures for diagnostic evaluation, and only those in which VRF line was directly confirmed intraoperatively were classified as VRF root. To minimize confounding effects related to anatomical superimposition, the study included only mandibular premolars and molars. For each VRF root, one matched control root was selected from the same patient. Cases without an appropriate within-patient match were excluded. Usually, either the nearest adjacent premolar or molar, or a contralateral mandibular premolar or molar of the same root type was selected. Control roots were defined as teeth without clinical or radiographic findings suggestive of VRF. These roots demonstrated a periodontal probing depth of less than 3 mm at all measured sites, with no evidence of localized deep periodontal pocketing or sinus tract formation. Radiographically, control root showed no fracture-related alveolar bone loss and no periapical radiolucency indicative of active endodontic pathology on panoramic radiographs. Exclusion criteria comprised generalized periodontitis or horizontal alveolar bone loss, periapical radiolucency unrelated to VRF, inadequate image quality due to severe motion artifacts, absence of an appropriate matched control root, and teeth with advanced root splitting or complete fragment separation that could obscure early trabecular bone texture alterations.

2.2 Imaging protocol and image preprocessing

All panoramic radiographs were acquired using a digital panoramic system (Orthopantomograph OP 200D, Instrumentarium Dental, Tuusula, Finland) equipped with a direct digital detector. Images were obtained according to the manufacturer's standard clinical protocol using routine exposure parameters optimized for adult patients. All images were exported in Digital Imaging and Communications in Medicine (DICOM) format from the

institutional Picture Archiving and Communication System (PACS) without any additional post-processing. The original panoramic DICOM images consisted of 12-bit grayscale values ranging from 0 to 4095. Raw pixel intensity values provided in the DICOM files were used directly for all analyses. No additional image enhancement procedures, including histogram equalization, brightness or contrast adjustment, gamma correction, or noise filtering, were applied in order to preserve the original gray-level distribution and to minimize artificial distortion of intrinsic texture characteristics.

2.3 Texture analysis

The analysis pipeline followed a workflow consisting of ROI selection, fixed gray-level discretization, and feature extraction, with identical parameters applied across all ROIs and subjects (Figure 1). All texture analyses were implemented using custom-written scripts in MATLAB (R2024a, MathWorks, Natick, MA, USA). Image assessment and ROI placement were performed using a calibrated 21.2-inch diagnostic monitor (WIDE CX30p, 3-megapixel color LED diagnostic monitor; WIDE Medical, Gyeonggi-do, Korea) under standardized viewing conditions. Texture analysis was performed at the root level using complementary descriptors to characterize trabecular bone microarchitecture, including GLCM features, FD, and lacunarity.

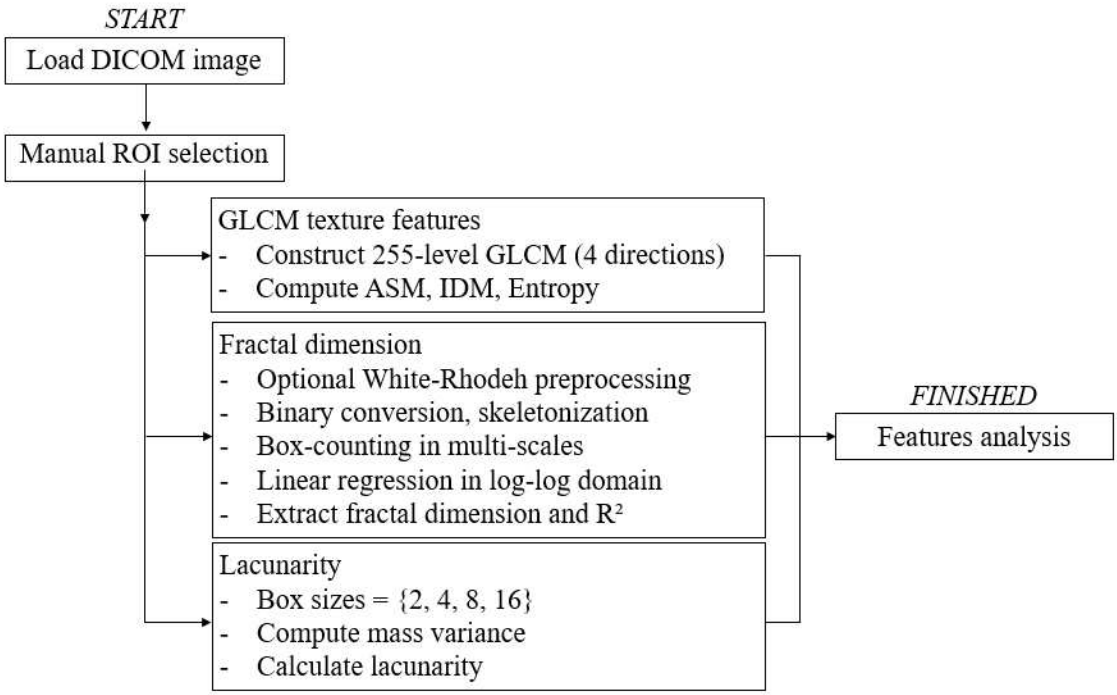


Figure 1. Overview of the ROI-based texture analysis workflow.

Panoramic DICOM images were loaded and standardized regions of interest (ROIs) in the trabecular bone adjacent to the analyzed root were manually selected. Texture features were extracted through three analytical pathways: gray-level co-occurrence matrix (GLCM)–based features, fractal dimension, and lacunarity. All extracted features were subsequently subjected to statistical analysis.

Abbreviations: DICOM, digital imaging and communications in medicine; ROI, region of interest; GLCM, gray-level co-occurrence matrix; ASM, angular second moment; IDM, inverse difference moment.

2.3.1 ROI definition and positioning

Seven anatomically standardized square ROIs (20 × 20 pixels) were defined along the long axis of each analyzed root to capture vertical and lateral variations in trabecular bone texture.

(Figure 2). ROIs were placed at the alveolar crest level on the mesial and distal sides (AC-M, AC-D), at the mid-alveolar bone level (MID-M, MID-D), and within the periapical trabecular region (PERI-M, PERI-D), with an additional ROI positioned at the center of the root apex (APEX). This mesial–distal paired design was adopted to account for potential asymmetry in load transmission and bone remodeling around the root. All ROIs were carefully positioned on trabecular bone immediately adjacent to the root surface while avoiding overlap with the root structure, periodontal ligament space, cortical bone, or adjacent anatomical boundaries. In mandibular molars with two roots, mesial and distal roots were evaluated independently; when VRF was confined to a single root, only ROIs surrounding the fractured root were included. This root-level approach was intentionally applied to prevent dilution of texture characteristics by uninvolved roots and to ensure that extracted features accurately reflected localized trabecular alterations associated with the fractured root. ROIs were manually defined by two independent observers (S.-M.H., a periodontist, and Y.-E.K., an oral and maxillofacial radiologist), each with more than 10 years of professional experience, using MATLAB-based image analysis tools. All ROIs were delineated under identical imaging conditions. Each examiner repeated the ROI placement procedure three times at one-week intervals, and feature values were averaged across the three repeated placements. For primary analyses, the averaged values from the two observers were further averaged ($k = 2$). Both examiners were blinded to the clinical diagnosis and group allocation. All three analytical pathways, GLCM texture features, fractal dimension, and lacunarity, were derived independently from the same ROI, with no dependency on the output of one another. Consequently, the analyses could be performed sequentially, separately, or in parallel by design, without affecting the extracted feature values.

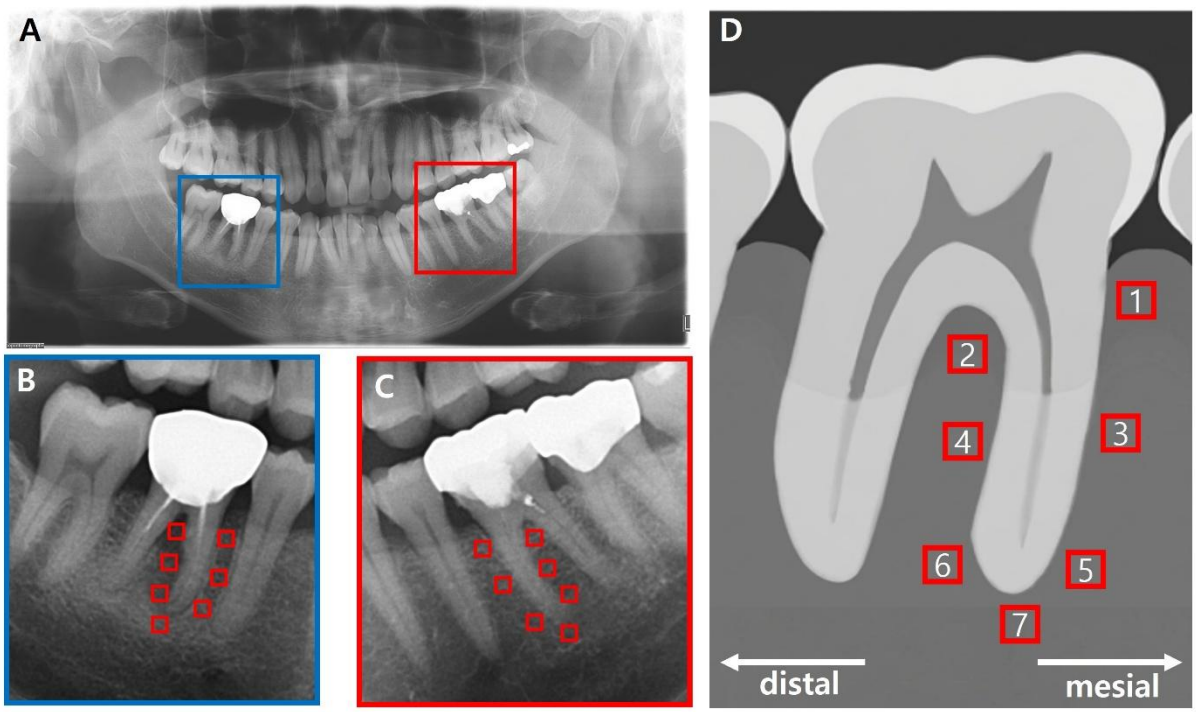


Figure 2. Standardized ROI placement for the trabecular texture analysis.

(A) Panoramic radiograph showing a VRF tooth (blue box) and a matched control tooth (red box). (B) Enlarged view of the normal control root with standardized square ROIs placed on the periradicular trabecular bone. (C) Enlarged view of the VRF root with identical ROI placement. (D) Schematic representation of the seven anatomically defined ROIs along the root axis: AC-M (1), AC-D (2), MID-M (3), MID-D (4), PERI-M (5), PERI-D (6), and APEX (7).

Abbreviations: ROI, region of interest; VRF, vertical root fracture

2.3.2 GLCM-based texture features

GLCMs were calculated using MATLAB built-in function *graycomatrix*(·). Prior to the

computation of GLCM features, pixel intensities within each ROI were normalized by dividing each value by the maximum intensity. This normalization step was applied solely for numerical scaling and did not alter relative gray-level relationships within the image. For GLCM construction, normalized ROI intensities were discretized into 255 gray levels using a fixed bin number. This uniform discretization scheme was consistently applied across all ROIs in accordance with commonly adopted and Image Biomarker Standardisation Initiative (IBSI)-recommended radiomics discretization practices, thereby ensuring feature comparability and reproducibility between subjects and between VRF and control roots.

The ROI intensities were first quantized into 255 fixed gray levels to ensure a consistent intensity discretization. GLCMs were generated in four orientations, such as 0, 45°, 90°, and 135°, with an inter-pixel distance of one pixel. A symmetric co-occurrence formulation was applied so that the probability of observing pixel pairs (i,j) and (j,i) was merged into a single estimate. The four directional matrices were then averaged to obtain a directionally invariant representation of local spatial dependence. From this averaged GLCM, $P(i,j)$, classical Haralick features were computed[21]. Contrast, angular second moment (ASM), inverse difference moment (IDM), and entropy were defined as follows[22]:

$$Contrast = \sum_{i,j}(i-j)^2 P(i,j), \qquad ASM = \sum_{i,j} P(i,j)^2,$$

$$IDM = \sum_{i,j} \frac{P(i,j)}{1+|i-j|}, \; Entropy = -\sum_{i,j} P(i,j) log_2 P(i,j). \qquad (1)$$

Contrast describes the degree of local intensity variation. ASM measured uniformity within the ROIs. IDM quantified the similarity of neighboring intensities. Entropy reflects the degree of randomness within the local texture. Small probability values were replaced with ε to avoid

undefined logarithms.

2.3.3 FD-based texture features

FD characteristics were assessed using a box-counting approach applied to each ROI. To enhance trabecular-like structural patterns, the ROI underwent Gaussian blurring with standard deviation of 3, followed by subtraction from the original image, min–max normalization, binary thresholding, morphological cleaning, and skeletonization. The binarized image was skeletonized to obtain a simplified representation of the underlying structural complexity. Box counting was then performed across dyadic scales, and the number of occupied boxes at each scale, denoted as $N(s)$, was calculated[25]. FD was obtained from the slope of the linear regression between $logN(s)$ and $log(1/s)$.

$$logN(s) = -(FD)log(s) + C \qquad (2)$$

The intercept C represents only the constant term arising from the number of occupied boxes at the smallest scale (s=1). Model fit was quantified using the coefficient of determination as follows:

$$R^2 = 1 - \frac{SS_{res}}{SS_{tot}} \qquad (3)$$

where SS_{res} is the residual sum of squares and SS_{tot} is the total sum of squares. The relationship between the two quantities forms the basis of the coefficient of determination, R^2, which compares the unexplained variability to the total variability. When SS_{res} is small relative to SS_{tot}, the regression line accounts for most of the observed variation, and the resulting R^2 value approaches unity, indicating a strong fractal scaling relationship.

2.3.4 Lacunarity-based texture features

Structural heterogeneity was additionally evaluated through lacunarity analysis. For this measure, each ROI was divided into blocks of increasing size (2, 4, 8, and 16 pixels), and the mass of each block, defined as the sum of its pixel values, was computed. The distribution of block masses was summarized by its mean (μ) and standard deviation (σ). The Lacunarity is calculated as:

$$\Lambda = \left(\frac{\sigma}{\mu}\right)^2 + 1 \qquad (4)$$

It captured the degree of spatial irregularity and the presence of structural gaps across scales. The final lacunarity value for each ROI was obtained by averaging across all block sizes.

All three analytical pathways, including GLCM texture extraction, fractal-dimension estimation, and lacunarity computation, operated independently on the same ROI and did not rely on the output of one another. Therefore, they could be executed sequentially, separately, or in parallel without altering the resulting feature values. The complete feature vector for each ROI consisted of contrast, ASM, IDM, entropy, FD, and lacunarity, collectively describing the texture, complexity, and heterogeneity of the underlying anatomical structures.

2.4 Statistical analysis

Inter-observer reliability was assessed using the intraclass correlation coefficient (ICC) based on a two-way random-effects model with absolute agreement. ICC(2,1) and ICC(2,k) were calculated for single and average measurements, respectively, with 95% confidence intervals. Agreement between observers was further evaluated using Bland–Altman analysis to assess mean bias and 95% limits of agreement. Texture features were compared on a paired basis between VRF roots and control roots. Normality of paired differences was assessed using the Shapiro–Wilk test. For normally distributed data, paired t-tests were applied, whereas the

Wilcoxon signed-rank test was used for non-normally distributed data. Feature values were summarized as mean ± standard deviation, and region-wise analyses were performed to evaluate spatial variation in texture alterations along the root axis. To facilitate comparison across features with different scales, standardized z-scores and relative percentage changes (Δ% = [(VRF − control)/control] × 100) were calculated for descriptive and comparative interpretation. Inter-feature relationships within the VRF and control groups were examined using Pearson correlation coefficients as an exploratory analysis and visualized using correlation matrices. Most statistical analyses, including paired group comparisons and ICC estimation, were performed using R software (version 4.5.1; R Foundation for Statistical Computing, Vienna, Austria), with statistical significance set at $p < 0.05$. Pearson correlation was performed using GraphPad Prism (version 10.0; GraphPad Software, Inc., San Diego, CA, USA).

Results

3.1 Patient characteristics

This retrospective study included 38 patients (26 males and 12 females; mean age, 63.8 ± 10.3 years; range, 44–86 years). A total of 40 VRF roots were identified, and 40 matched control roots were selected for comparison. The distribution of root types for both groups is presented in Table 1. Clinical symptoms and treatment histories are summarized in Table 2. In the VRF group, pain was the most common presenting symptom, either alone (42.5%) or in combination with swelling (27.5%), while 17.5% of VRF teeth were asymptomatic at the time of diagnosis. Regarding treatment history, VRF roots showed a predominance of combined treatment modalities (57.5%). Endodontic therapy was the most frequent form of treatment, followed by crown restoration. In contrast, control roots were more often untreated (45.0%) or had received

only conservative treatment.

Table 1. Patient demographics and root distribution.

Characteristic	Value
Number of patients	38*
Sex (Male/Female)	26 / 12
Age (years)	
Mean ± SD	63.8 ± 10.3
Range	44–86
Control root (*n = 40*)	
1st premolar (#34, 44) †	4 (10.0%)
2nd premolar (# 35, 45) †	7 (17.5%)
1st molar (#36, 46) †	24 (60.0%)
2nd molar (# 37, 47) †	11 (27.5%)
VRF root (*n = 40*)	
1st premolar (#34, 44) †	0 (0%)
2nd premolar (# 35, 45) †	1 (2.5%)
1st molar (#36, 46) †	19 (47.5%)
2nd molar (# 37, 47) †	11 (27.5%)

*Two female patients contributed bilateral VRF roots

† Tooth numbers are presented according to the FDI notation system

Abbreviations: SD, standard deviation; VRF, vertical root fracture; FDI, Fédération Dentaire Internationale

Table 2. Clinical symptoms and treatment status of VRF and control root

Category	Control root (*n* = 40)	VRF root (*n* = 40)
P only	–	17 (42.5%)
P + S	–	11 (27.5%)
P + pus	–	1 (2.5%)
N	–	7 (17.5%)
Total symptoms	–	40 (100%)
Treatment status		
No treatment	18 (45.0%)	8 (20.0%)
Single treatment		

Category	Control root (n = 40)	VRF root (n = 40)
R only	8 (20.0%)	5 (12.5%)
C only	5 (12.5%)	4 (10.0%)
Subtotal — Single	13 (32.5%)	9 (22.5%)
Combined treatment		
E + C	9 (22.5%)	19 (47.5%)
E + Po + C	0	4 (10.0%)
Subtotal — Combined	9 (22.5%)	23 (57.5%)
Total (treatment)	40 (100%)	40 (100%)

Abbreviations: P, pain; S, swelling; N, asymptomatic; R, restorative treatment (resin or inlay); E, endodontic treatment; Po, post; C, crown restoration

3.2 ROI reliability

Inter-observer reliability of texture feature extraction across the seven anatomically standardized ROIs was evaluated using ICC and Bland–Altman analysis (Figures 3, 4, and S1). Raw texture feature values used for reliability assessment are provided in Table S1. Overall, ASM, IDM, and entropy demonstrated excellent inter-observer agreement across most ROIs, with ICC values predominantly exceeding 0.75 for both single measurements [ICC(2,1)] and averaged measurements [ICC(2,k)]. Contrast, FD, and lacunarity exhibited moderate-to-good agreement, with ICC values generally ranging from approximately 0.60 to 0.80. Detailed ICC results, including ICC(2,1) and ICC(2,k), 95% confidence intervals, and coefficients of variation (CVs), are summarized in Table S2. Bland–Altman plots further supported these findings by demonstrating minimal mean bias and narrow limits of agreement for all six texture features, with the vast majority of paired measurements falling within the 95% limits of agreement (Figures 4 and S1).

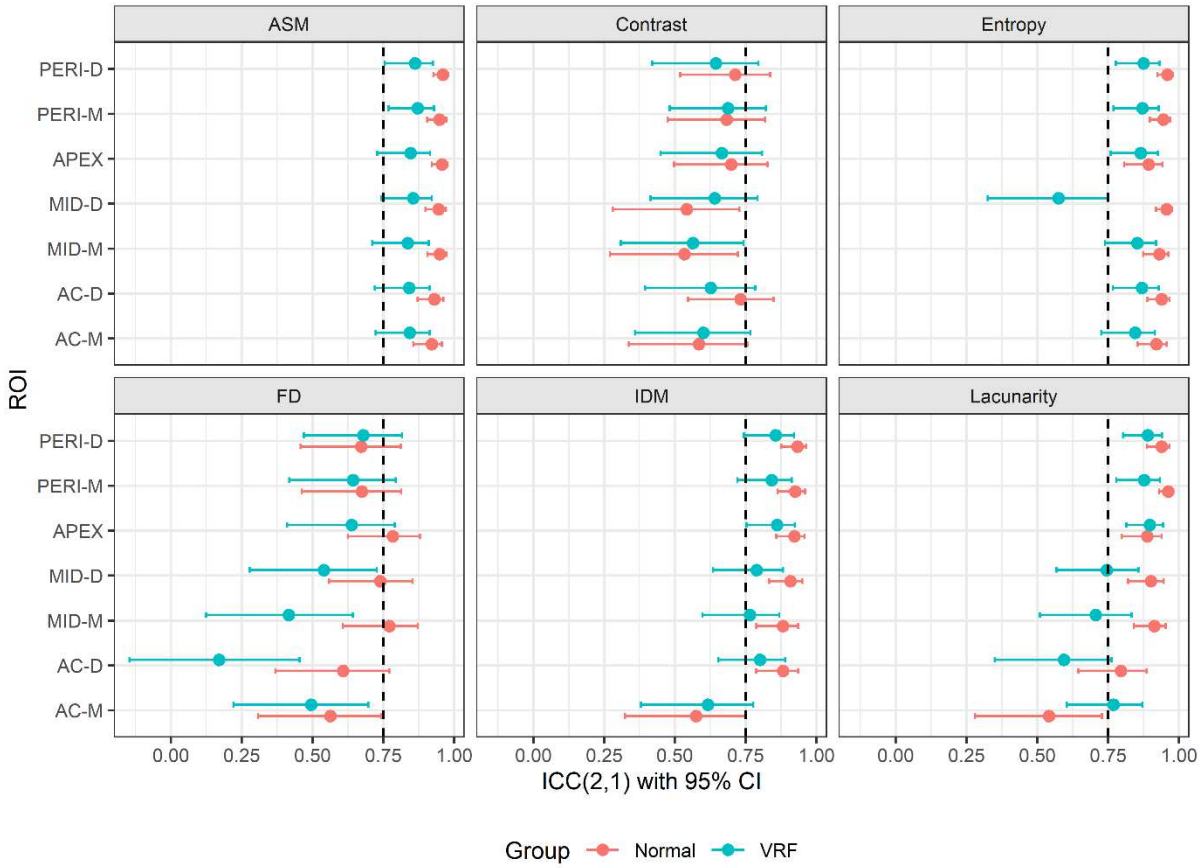


Figure 3. Inter-observer reliability of the ROI-based texture features.

ICC[2,1] with 95% confidence intervals are shown for six texture features (ASM, contrast, entropy, FD, IDM and lacunarity) across the seven predefined ROIs. ICC values are presented separately for normal control and VRF groups. The dashed vertical line indicates the threshold for good agreement (ICC = 0.75).

Abbreviations: ICC, intraclass correlation coefficients; ASM, angular second moment; FD, fractal dimension; IDM, inverse difference moment; ROI, region of interest; VRF, vertical root fracture

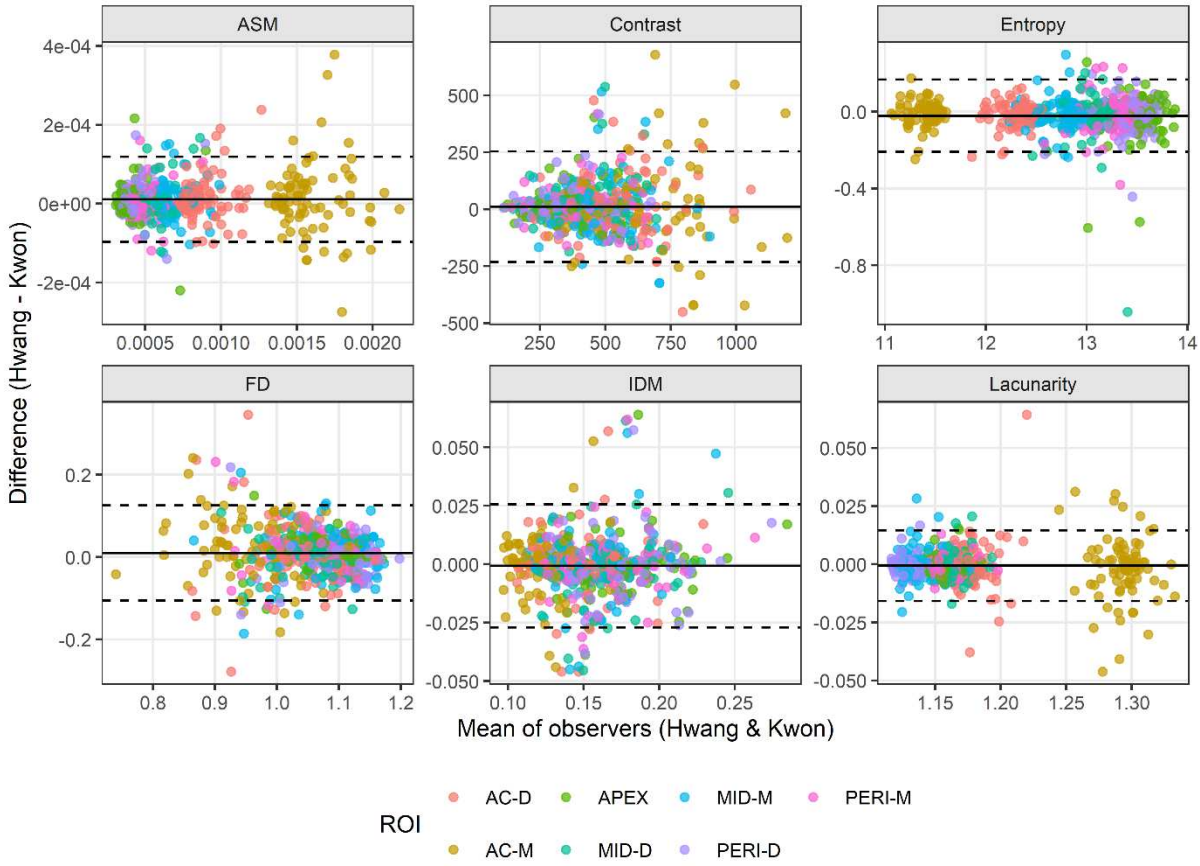


Figure 4. Bland–Altman analysis of the inter-observer agreement for texture features.

Bland–Altman plots showing agreement between two observers for six texture features across all predefined ROIs. The difference between observers (S.-M.H. – Y.-E.K.) is plotted against their mean value. The solid horizontal line represents the mean bias, and the dashed lines indicate the 95% limits of agreement. Points are color-coded according to ROI location.

Abbreviations: ROI, region of interest

3.3. ROI-based comparison between VRF and control group

ROI-based comparisons of texture features demonstrated consistent and spatially organized

differences in texture features between VRF and control roots across all seven ROIs (Figure 5A–C; Table 3). Standardized z-score analysis (Figure 5A) revealed that when all ROIs were averaged, the mean z-scores of each texture feature were located near zero, indicating substantial overlap in global texture distribution between the two groups. This suggests that global averaging attenuates potential regional signals. Relative percentage change (Δ%) analysis (Figure 5B) revealed that GLCM contrast and IDM exhibited the largest proportional differences between VRF and control groups. Further ROI-stratified raw feature distribution analysis (Figure 5C; Table 3) confirmed that, at the regional level, consistent directional changes were observed. Specifically, GLCM contrast decreased by approximately 11–29% across all ROIs, whereas IDM increased by approximately 14–19%, demonstrating a uniform pattern throughout the regions examined. These differences were statistically significant ($p < 0.001$). In contrast, lacunarity showed limited and region-specific changes, reaching statistical significance only in selected ROIs (AC-M, AC-D, PERI-D).

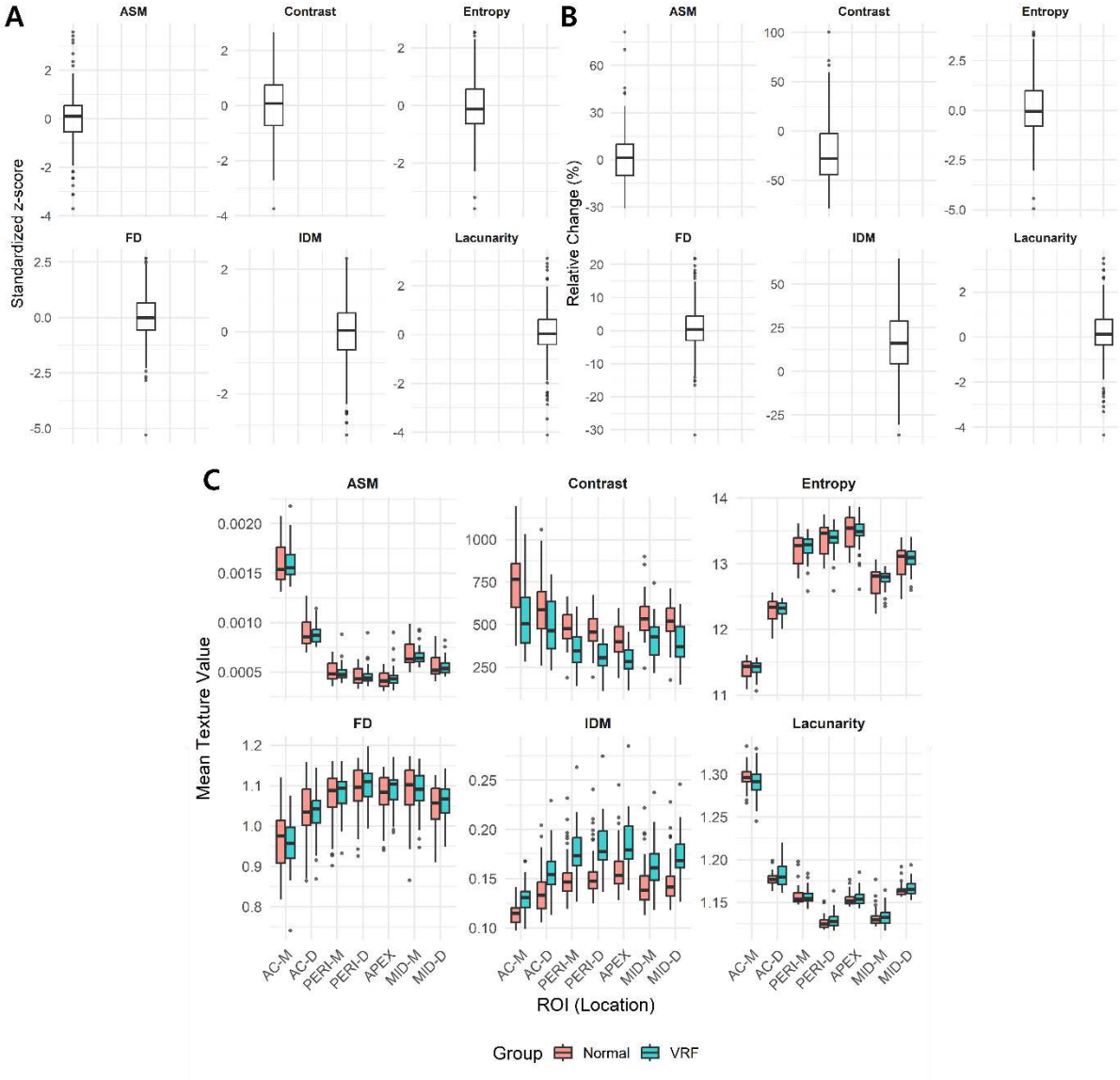


Figure 5. ROI-based regional differences in the texture features between VRF and normal teeth.

(A) Standardized z-scores of six texture features comparing VRF and normal groups across all predefined ROIs. (B) Relative percentage changes (Δ%) in texture features between VRF and normal groups for each ROI. (C) Distribution of raw texture feature values according to ROI location, shown separately for normal and VRF groups.

Abbreviations: VRF, vertical root fracture; ROI, region of interest

Table 3. ROI-based statistical comparison of texture features between control and VRF group

ROI	Feature	Δ (VRF − Control)	% Change	*p*-value	Significance
AC-D	ASM	0	-0.94	0.627	
AC-D	Contrast	-110.299	-11.41	0.0043	**
AC-D	Entropy	0.03	0.26	0.519	
AC-D	FD	-0.008	-0.52	0.471	
AC-D	IDM	0.018	15.52	0.000418	***
AC-D	Lacunarity	0.005	0.46	0.0109	*
AC-M	ASM	0	0.97	0.952	
AC-M	Contrast	-201.944	-23.72	0.000000641	***
AC-M	Entropy	-0.001	0	0.966	
AC-M	FD	-0.004	0.23	0.984	
AC-M	IDM	0.015	14.24	0.00000162	***
AC-M	Lacunarity	-0.006	-0.48	0.0163	*
APEX	ASM	0	8.1	0.132	
APEX	Contrast	-113.516	-24.13	0.00000489	***
APEX	Entropy	-0.044	-0.31	0.243	
APEX	FD	0.009	0.98	0.135	
APEX	IDM	0.025	16.9	0.00000805	***
APEX	Lacunarity	0.002	0.14	0.388	
MID-D	ASM	0	-1.6	0.195	
MID-D	Contrast	-137.113	-23.76	0.000000958	***
MID-D	Entropy	0.058	0.46	0.0555	
MID-D	FD	0.011	1.27	0.189	
MID-D	IDM	0.023	17.24	0.0000104	***
MID-D	Lacunarity	0.002	0.19	0.206	

ROI	Feature	Δ (VRF − Control)	% Change	*p*-value	Significance
MID-M	ASM	0	-2.5	0.216	
MID-M	Contrast	-133.172	-21.07	0.00000847	***
MID-M	Entropy	0.048	0.39	0.265	
MID-M	FD	0.001	0.37	0.959	
MID-M	IDM	0.019	15.34	0.0000593	***
MID-M	Lacunarity	0.001	0.12	0.248	
PERI-D	ASM	0	3.2	0.695	
PERI-D	Contrast	-145.935	-28.92	0.0000000926	***
PERI-D	Entropy	-0.001	0.01	0.985	
PERI-D	FD	0.011	1.16	0.155	
PERI-D	IDM	0.027	19.18	0.000000906	***
PERI-D	Lacunarity	0.003	0.29	0.0224	*
PERI-M	ASM	0	0.02	0.577	
PERI-M	Contrast	-130.628	-24.42	0.000000993	***
PERI-M	Entropy	0.028	0.23	0.383	
PERI-M	FD	0.011	1.22	0.243	
PERI-M	IDM	0.024	17.35	0.00000718	***
PERI-M	Lacunarity	-0.001	-0.06	0.984	

[*] *Paired comparisons between control and VRF roots were performed for each ROI and feature. Paired t-tests or Wilcoxon signed-rank tests were applied depending on the normality of paired differences.*
** $p < 0.05$; **$p < 0.01$; ***$p < 0.001$*

Abbreviations: ASM, angular second moment; FD, fractal dimension; IDM, inverse difference moment; ROI, region of interest; VRF, vertical root fracture

3.4 Inter-feature relationships

Correlation analysis revealed distinct differences in the inter-feature relationship between the control and VRF groups (Figure 6). Although the absolute FD values did not differ significantly

between groups, a redistribution of correlation patterns among texture features was observed in the VRF group. In particular, changes in correlation coefficients involving FD reached a meaningful magnitude based on effect size interpretation. Specifically, associations between FD and ASM, contrast, entropy, and IDM demonstrated moderate (Δr = 0.20–0.30) shifts compared with the control group.

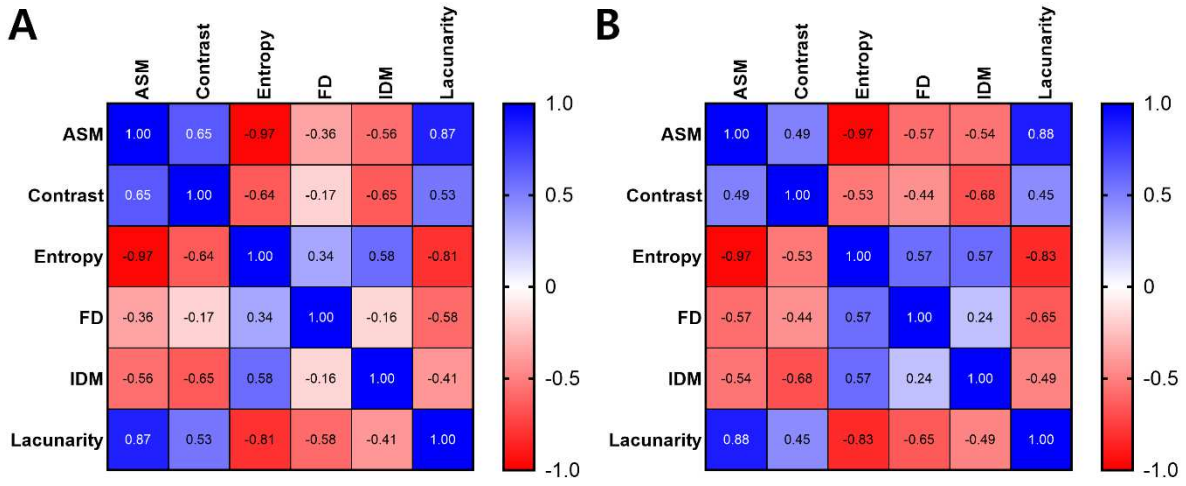


Figure 6. Correlation structure of the texture features in normal and VRF groups.

Heatmaps showing Pearson correlation coefficients among six texture features in the normal control (A) and VRF (B) groups. Blue indicates positive correlations and red indicates negative correlations.

Abbreviations: VRF, vertical root fracture

Discussion

The present study demonstrated that panoramic radiograph–based quantitative texture analysis

can detect subtle alterations in the trabecular bone microstructure surrounding VRF roots. By applying ROI-level texture feature extraction across anatomically standardized regions, we identified spatially organized and statistically significant differences between VRF and matched control roots.

In this study, control roots were defined based on the absence of clinical or radiographic signs suggestive of VRF or active endodontic/periodontal pathology, rather than the absence of prior dental treatment. As shown in Table 2, a proportion of control teeth had histories of restorative or prosthetic procedures, reflecting typical clinical conditions rather than completely untreated teeth. While the VRF group demonstrated a higher frequency of prior endodontic/prosthetic treatments, this association should be interpreted cautiously as a clinical characteristic rather than a direct causal factor. The presence of treated yet non-fractured control teeth suggests that additional anatomical or biomechanical factors may contribute to VRF development[6–8].

Inter-observer reliability was assessed using the ICC and Bland–Altman analysis (Figure 3,4 and S1). The majority of paired measurements were distributed close to the line of equality, indicating good agreement between the two observers. These findings support the overall reproducibility of the ROI selection and texture feature extraction process.

As shown in Figures 5 and 6 and Table 3, integration of the present findings suggests that the decrease in contrast observed in the VRF group reflects attenuation of trabecular boundary definition and reduced local intensity variation within the ROI. In parallel, the increase in IDM indicates greater local homogeneity of bone structure, which can be interpreted as a complementary pattern to the reduction in contrast. In contrast, the relatively small changes observed in FD, entropy, and lacunarity may indicate that VRF-related alterations are localized and potentially confined to early microstructural remodeling rather than representing

widespread architectural disruption. Furthermore, the two-dimensional projection nature of panoramic imaging may attenuate subtle three-dimensional structural differences, leading to limited separation in global texture metrics.

Previous studies have approached VRF detection primarily from a radiographic sign–based or direct fracture identification perspective. Kawamura-Hagiya et al.[8] developed a logistic regression model based on observable radiographic signs in periapical images to screen for VRF. Their approach relied on predefined qualitative radiographic features to construct a predictive statistical model. In contrast, the present study employed quantitative texture feature–based analysis, focusing on the microarchitectural bone pattern surrounding the fractured root rather than visually identifiable radiographic signs. Similarly, Fukuda et al.[11] applied a convolutional neural network (CNN) model to detect clearly progressed split-tooth cases, aiming to directly identify fracture lines. While this deep learning–based approach targets overt structural discontinuities, the current study differs in both diagnostic stage and analytical focus. Rather than detecting explicit fracture lines, we quantified trabecular bone alterations adjacent to VRF roots, thereby exploring subtle periradicular microstructural changes that may precede or accompany radiographically evident fractures. This distinction highlights the methodological and conceptual difference between fracture-line detection and bone microstructure–based quantitative pattern analysis.

From biological and biomechanical perspectives, this pattern likely reflects the combined effects of fracture-related stress redistribution and biologically driven bone remodeling during VRF progression[6, 14, 16]. As microcracks propagate along the root surface, abnormal stress concentrations develop in the surrounding alveolar bone, promoting microdamage accumulation and disrupting the balance between osteoclastic resorption and compensatory

bone formation[6, 14, 16]. This imbalance results in spatially heterogeneous remodeling, in which trabecular rarefaction and structural disruption coexist with reactive bone deposition[14, 15]. At the feature level, increased fractal dimension denotes greater trabecular complexity and fragmentation, while elevated lacunarity and entropy indicate irregular marrow space enlargement and non-uniform bone loss[14, 15, 26, 27]. Concurrent reductions in uniformity-related metrics and contrast flattening correspond to loss of coherent gray-level transitions and trabecular alignment[14, 26]. Collectively, these feature-level alterations reflect microarchitectural reorganization of the alveolar bone under chronic mechanical and inflammatory stress[14].

Recent literature[15, 17, 20, 24, 28–30] has consistently demonstrated that texture analysis can be applied to panoramic radiographs to provide a meaningful and objective surrogate for assessing trabecular bone microarchitecture across a wide range of clinical and biological conditions. FD analysis, in particular, has been repeatedly shown to sensitively capture alterations in trabecular complexity and spatial organization on panoramic images, reflecting underlying changes in bone remodeling associated with periodontal disease, endodontic treatment, implant loading, systemic bone loss, and functional disuse, even when conventional radiographic density changes are subtle or absent[15, 17, 20, 24, 28]. Beyond FD alone, complementary texture metrics, such as lacunarity, have been shown to characterize the heterogeneity and spatial distribution of trabecular voids, providing additional discriminatory power in conditions where overall structural complexity may overlap between groups, including tobacco exposure and systemic osteoporosis screening on panoramic radiographs[28, 29]. Second-order statistical approaches, including GLCM features, further enable quantitative characterization of trabecular uniformity, contrast, and disorder, allowing panoramic-based

texture analysis to capture coordinated multivariate patterns of bone alteration rather than isolated univariate changes[30]. Importantly, these methodological advances have been applied across diverse research questions, ranging from systemic bone health assessment and osteoporosis screening to localized biomechanical adaptation following endodontic therapy, prosthodontic loading, and implant osseointegration[15, 20, 24]. These observations underscore the versatility of panoramic texture analysis as a low-dose, widely available imaging platform[15, 20, 24]. The consistent ability of panoramic texture features to discriminate between clinically distinct groups, even in the presence of overlapping radiographic density or treatment histories, supports their role as objective imaging features that reflect biologically relevant trabecular reorganization rather than mere projection-related artifacts[17, 28, 30]. Taken together, prior evidence indicates that panoramic radiograph–based texture analysis, when performed using standardized ROI placement and validated computational pipelines, represents a clinically relevant approach for indirect assessment of trabecular bone quality. These findings provide a methodological and conceptual foundation for the present study, which extends this framework to the detection of VRF-associated trabecular alterations, further highlighting the diagnostic potential of panoramic texture analysis in routine dental imaging.

In the context of VRF diagnosis, most previous imaging studies have emphasized direct or indirect visualization of fracture lines using CBCT or, more recently, AI-based detection frameworks[3, 7, 10, 11, 31]. While CBCT provides three-dimensional structural information, its diagnostic performance may be limited by beam-hardening artifacts, metal-related distortions, and relatively higher radiation exposure, particularly in teeth with posts or extensive restorations[6, 7, 10, 11, 31]. AI-based approaches have shown promising results, but

often rely on clearly visible fracture features or large, well-annotated datasets, which may limit applicability in early or ambiguous cases[13, 15–17, 24, 27, 30, 32]. By contrast, the present study adopted a complementary paradigm by focusing on the quantitative analysis of peri-radicular trabecular bone texture derived from routinely acquired, low-dose panoramic radiographs[11, 13, 15–17, 24, 32]. By capturing subtle, distributed microarchitectural changes rather than relying on direct fracture visualization, this approach may complement existing CBCT- and AI-based strategies and offers potential as a non-invasive, low-radiation screening adjunct for VRF detection[1, 8, 13–15, 17–19, 27, 32, 33].

From a clinical perspective, the findings suggest that texture- and fractal-based analysis may have potential as an adjunctive analytical layer when applied to routine panoramic radiographs in the assessment of teeth suspected of VRF. Rather than serving as a standalone diagnostic tool, this approach could be explored as part of a targeted screening strategy to identify teeth that may warrant closer clinical observation or further imaging evaluation.

This study has several limitations. The retrospective design of this study and the involvement of a single institution with a relatively limited sample size may restrict the generalizability of the findings. The analysis focused on mandibular premolars and molars under anatomically and radiographically controlled conditions. Although this design choice aimed to minimize confounding effects related to anatomical superimposition and panoramic projection geometry, the immediate applicability of the results to maxillary teeth or anterior regions, where trabecular patterns and image distortion characteristics differ, may be limited. Our texture analysis relied on manually defined ROIs, which, despite demonstrating acceptable inter-observer reliability, may still introduce a degree of operator-dependent variability. Moreover, inherent limitations of panoramic radiography, including lower spatial resolution, geometric

distortion, and its two-dimensional representation of three-dimensional trabecular microarchitecture, should be considered when interpreting the texture-derived parameters. VRF diagnosis was established using accepted reference standards, such as surgical exploration and CBCT findings. However, the possibility of residual selection bias cannot be entirely excluded.

Future studies should aim to validate the present findings using larger, multicenter datasets, and to extend the analysis to additional tooth regions with region-specific optimization of ROI definition. In particular, future studies should determine whether the texture-based features identified in this study can assist in differentiating VRF-related trabecular alterations from other conditions with overlapping radiographic appearances, such as early periapical lesions or initial periodontal bone changes. Comparative analyses across these entities may help clarify the specificity and clinical relevance of the proposed texture patterns. Furthermore, future studies could extend the present ROI-based texture analysis into a radiomics-oriented framework by incorporating automated or semi-automated pipelines, including robust feature selection and classification models. Building upon the statistically validated texture differences identified in this study, radiomics-based modeling may enable the integration of multiple complementary features to predict VRF status in previously unseen panoramic radiographs. Additionally, machine learning or AI-assisted approaches may enhance reproducibility, reduce observer dependency in the definition of ROI, and facilitate clinical scalability by enabling objective, data-driven decision support. Nevertheless, VRF is a heterogeneous condition influenced by both local structural changes and clinical factors, suggesting that a single-modality imaging approach may not fully reflect its diagnostic complexity. Integration of panoramic texture features with CBCT findings, clinical symptoms, and treatment history

could ultimately support the development of a multimodal diagnostic framework for more comprehensive VRF risk assessment.

This study demonstrated that ROI-based texture analysis of panoramic radiographs characterized spatially organized trabecular bone alterations associated with VRF, even in the absence of a clearly visible fracture line. These findings suggest that quantitative texture-based features derived from routinely acquired panoramic radiographs may offer complementary information for future VRF screening and diagnostic assessment.

Supplementary Materials

The following supporting information can be downloaded online:

Figure S1. Scatter plots of the inter-observer agreement for texture features. Scatter plots comparing texture feature values measured by two observers (S.-M.H. and Y.-E.K.) for six texture features across all predefined ROIs. Each point represents a single ROI measurement. The dashed line indicates the line of identity (y = x). Points are color-coded according to ROI location.

Abbreviations: ROI, region of interest

Table S1. **Raw texture feature values used for inter-observer reliability assessment.** Observer-specific texture feature values extracted from seven anatomically standardized square ROIs (20 × 20 pixels) placed along the long axis of each analyzed root (AC-M, AC-D, MID-M, MID-D, PERI-M, PERI-D, and APEX) in VRF-affected roots and matched control roots. For each subject, ROI, and group (Normal vs. VRF), values are provided separately for the two independent observers. The reported features include GLCM-based metrics (contrast, ASM, IDM, and entropy), FD, and lacunarity.

Abbreviations: ASM, angular second moment; FD, fractal dimension; IDM, inverse difference moment; ROI, region of interest; VRF, vertical root fracture

Table S2. **Inter-observer reliability of texture features across ROIs assessed by ICC.** Inter-observer reliability for each texture feature and ROI is summarized using ICCs derived from a two-way random-effects model with absolute agreement. ICC(2,1) represents the reliability of a single observer's measurement, and ICC(2,k) represents the reliability of the average of observers (k = 2). ICCs are reported separately for the Normal and VRF groups with 95%

confidence intervals. CV indicates coefficient of variation (%), and n indicates the number of roots analyzed per group.

Abbreviations: ICC, intraclass correlation coefficients; ROI, region of interest; VRF, vertical root fracture; CV, coefficient of variation

Acknowledgements

Not applicable.

Funding

This work was supported by Kyungpook National University Dental Hospital Institute for Dental Research (2025)

Conflicts of Interest

The authors declare that they have no conflict of interest.

Ethics approval

This study was approved by the Kyungpook National University Dental Hospital Institutional Review Board (IRB No. KNUDH-2025-07-05-00) and was conducted in accordance with the Declaration of Helsinki.

Consent to participate

The requirement for informed consent was waived by the Kyungpook National University Dental Hospital Institutional Review Board (IRB No. KNUDH-2025-07-05-00) due to the retrospective nature of the study and the use of anonymized data.

Data Availability Statement

The datasets generated and/or analyzed during the current study are available from the corresponding author upon reasonable request. Access will be provided in accordance with institutional and ethical requirements.

Author Contributions

K.S.K contributed to the design of the image analysis methodology and performed the statistical analysis and data interpretation, and participated in critical revision of the manuscript for important intellectual content. S.-M.H contributed to the conception and overall design of the study, acquisition of clinical data, and interpretation of clinical findings, and participated in drafting and critical revision of the manuscript; S.-M.H also takes responsibility for the integrity of the work. Y.J.L contributed to the development and validation of the quantitative image analysis framework and interpretation of analytical results, and participated in critical revision of the manuscript for important intellectual content. Y.-E.K contributed to the conception of the study, radiologic interpretation of imaging data, and supervision of the imaging analysis process, and participated in drafting of the manuscript; Y.-E.K agrees to be accountable for all aspects of the work. All authors approved the final version of the manuscript.

Abbreviations

The following abbreviations are used in this manuscript:

ASM, angular second moment; CBCT, cone-beam computed tomography; CNN, convolutional neural network; CV, coefficient of variation; DICOM, Digital Imaging and Communications in Medicine; FD, fractal dimension; GLCM, gray-level co-occurrence matrix; ICC, intraclass correlation coefficient; IDM, inverse difference moment; PACS, Picture Archiving and Communication System; ROI, region of interest; SD, standard deviation; VRF, vertical root fracture.

Reference

1. LE Soares, DQ Freitas, KLD Lima, LR Silva, FP Yamamoto-Silva, and MADC Vieira. Application of image processing techniques to aid in the detection of vertical root fractures in digital periapical radiography. Clin Oral Invest. 2021;25:5077–85 https://doi.org/10.1007/s00784-021-03820-z

2. M Varshosaz, MA Tavakoli, M Mostafavi, and AA Baghban. Comparison of conventional radiography with cone beam computed tomography for detection of vertical root fractures: an in vitro study. J Oral Sci. 2010;52:593–7 https://doi.org/10.2334/josnusd.52.593

3. Z Hu, D Cao, Y Hu, B Wang, Y Zhang, R Tang, et al. Diagnosis of in vivo vertical root fracture using deep learning on cone-beam CT images. BMC Oral Health. 2022;22:382 https://doi.org/10.1186/s12903-022-02422-9

4. W-C Liao, Y-L Tsai, C-Y Wang, M-C Chang, W-L Huang, H-J Lin, et al. Clinical and Radiographic Characteristics of Vertical Root Fractures in Endodontically and Nonendodontically Treated Teeth. Journal of Endodontics. 2017;43:687–93 https://doi.org/10.1016/j.joen.2016.12.009

5. M Jasani, S Thakur, N Tn, and R Babannavar. Vertical root fractures: A scoping review. Int. J. Appl. Dent. Sci.. 2025;11:43–7 https://doi.org/10.22271/oral.2025.v11.i3a.2189

6. S Patel, B Bhuva, and R Bose. Present status and future directions: vertical root fractures in root filled teeth. Int Endodontic J. 2022;55:804–26 https://doi.org/10.1111/iej.13737

7. A Shokri, F Salemi, T Taherpour, H Karkehabadi, K Ramezani, F Zahedi, et al. Is cone-beam computed tomography more accurate than periapical radiography for detection of vertical root fractures? A systematic review and meta-analysis. BMC Med Imaging. 2024;24:286 https://doi.org/10.1186/s12880-024-01472-5

8. Y Kawamura-Hagiya, T Yoshioka, and H Suda. Logistic regression equation to screen for vertical root fractures using periapical radiographs. Dentomaxillofacial Radiology. 2008;37:28–33 https://doi.org/10.1259/dmfr/25198672

9. W Takeshita, LC Iwaki, M Da Silva, S Sabio, P Ricardo, and F Albino. Comparison of periapical radiography with cone beam computed tomography in the diagnosis of vertical root fractures in teeth with metallic post. J Conserv Dent. 2014;17:225 https://doi.org/10.4103/0972-0707.131781

10. DR Dias, LCV Iwaki, ACA De Oliveira, FS Martinhão, RM Rossi, MG Araújo, et al. Accuracy of High-resolution Small-volume Cone-Beam Computed Tomography in the Diagnosis of Vertical Root Fracture: An In Vivo Analysis. Journal of Endodontics. 2020;46:1059–66 https://doi.org/10.1016/j.joen.2020.04.015

11. M Fukuda, K Inamoto, N Shibata, Y Ariji, Y Yanashita, S Kutsuna, et al. Evaluation of an artificial intelligence system for detecting vertical root fracture on panoramic radiography. Oral Radiol. 2020;36:337–43 https://doi.org/10.1007/s11282-019-00409-x

12. KL De Lima, LR Silva, TB De Paiva Prado, MAG Silva, BS De Freitas Silva, and FP Yamamoto-Silva. Influence of the technical parameters of CBCT image acquisition on vertical root fracture diagnosis: a systematic review and meta-analysis. Clin Oral Invest. 2023;27:433–74 https://doi.org/10.1007/s00784-022-04797-z

13. JJ Hwang, J-H Lee, S-S Han, YH Kim, H-G Jeong, YJ Choi, et al. Strut analysis for osteoporosis detection model using dental panoramic radiography. Dentomaxillofacial Radiology. 2017;46:20170006 https://doi.org/10.1259/dmfr.20170006

14. BC Gonçalves, EC De Araújo, AD Nussi, N Bechara, D Sarmento, MS Oliveira, et al. Texture analysis of cone-beam computed tomography images assists the detection of furcal lesion. Journal of Periodontology. 2020;91:1159–66 https://doi.org/10.1002/JPER.19-0477

15. G Akay, U Pamukcu, and O Karadag Atas. Evaluation of the long-term structural change caused by root canal treatment in the bone around the tooth by fractal analysis. Oral Radiol. 2025;41:498–506 https://doi.org/10.1007/s11282-025-00825-2

16. MS Şimşek, H Alan, and N Dedeoğlu. A fractal evaluation study of implant-supported overdentures. Oral Surgery, Oral Medicine, Oral Pathology and Oral Radiology. 2025;140:264–70 https://doi.org/10.1016/j.oooo.2025.01.730

17. S Eser, and E Sarıbaş. Anatomical assessment of the trabecular structure of the alveolar bone in periodontal disease by fractal analysis method. Folia Morphol. 2024;83:157–67 https://doi.org/10.5603/FM.a2023.0023

18. MA Tayman, and E Sarıçam. Fractal Analysis of Trabecular Alveolar Bone with Intrabony and Furcation Defects Using Periapical Dental Radiographs. Eur J Ther. 2024; https://doi.org/10.58600/eurjther2121

19. P Soltani, S Sami, J Yaghini, E Golkar, F Riccitiello, and G Spagnuolo. Application of Fractal Analysis in Detecting Trabecular Bone Changes in Periapical Radiograph of Patients with Periodontitis. International Journal of Dentistry. 2021;2021:1–5 https://doi.org/10.1155/2021/3221448

20. N Dundar, E Aslan, and O Mutlu. Fractal dimension, lacunarity, and bone area fraction analysis of peri-implant trabecular bone after prosthodontic loading. Oral Radiol. 2025;41:120–30 https://doi.org/10.1007/s11282-024-00784-0

21. B Dhruv, N Mittal, and M Modi. Study of Haralick's and GLCM texture analysis on 3D medical images. International Journal of Neuroscience. 2019;129:350–62 https://doi.org/10.1080/00207454.2018.1536052

22. S Karri, S Aviel-Ronen, and MA Firer. Fractal and textural imaging identify new subgroups of patients with colorectal cancer based on biophysical properties of the cancer cells. Pathology - Research and Practice. 2022;238:154040 https://doi.org/10.1016/j.prp.2022.154040

23. MS Kavitha, S-Y An, C-H An, K-H Huh, W-J Yi, M-S Heo, et al. Texture analysis of mandibular cortical bone on digital dental panoramic radiographs for the diagnosis of

osteoporosis in Korean women. Oral Surgery, Oral Medicine, Oral Pathology and Oral Radiology. 2015;119:346–56 https://doi.org/10.1016/j.oooo.2014.11.009

24. E Soylu, A Coşgunarslan, S Çelebi, D Soydan, AE Demirbaş, and O Demir. Fractal analysis as a useful predictor for determining osseointegration of dental implant? A retrospective study. Int J Implant Dent. 2021;7:14 https://doi.org/10.1186/s40729-021-00296-0

25. T Cui, and T Wang. Exact box-counting and temporal sampling algorithms for fractal dimension estimation with applications to animal behavior analysis. Results in Engineering. 2025;25:103755 https://doi.org/10.1016/j.rineng.2024.103755

26. J Raja, M Khan, V Ramachandra, and O Al-Kadi. Texture analysis of CT images in the characterization of oral cancers involving buccal mucosa. Dentomaxillofacial Radiology. 2012;41:475–80 https://doi.org/10.1259/dmfr/83345935

27. S Mishra, M Kumar, L Mishra, S Panda, S Panda, N Lewkowicz, et al. Estimation of Cancellous Changes Using Fractal Analysis in Patients with Periodontitis. Biomedicines. 2023;11:2547 https://doi.org/10.3390/biomedicines11092547

28. L Pothuaud, E Lespessailles, R Harba, R Jennane, V Royant, E Eynard, et al. Fractal Analysis of Trabecular Bone Texture on Radiographs: Discriminant Value in Postmenopausal Osteoporosis. Osteoporosis International. 1998;8:618–26 https://doi.org/10.1007/s001980050108

29. S Basavarajappa, V Konddajji Ramachandra, and S Kumar. Fractal dimension and lacunarity analysis of mandibular bone on digital panoramic radiographs of tobacco users. J Dent Res Dent Clin Dent Prospects. 2021;15:140–6 https://doi.org/10.34172/joddd.2021.024

30. R Anandan, K C.L, A Ganesan, and Y Aniyan K. Strut and radio-morphometric analysis of mandibular trabecular structure in pre-and post-menopausal women to aid in the diagnosis of osteoporosis. Journal of Oral Biology and Craniofacial Research. 2024;14:273–9 https://doi.org/10.1016/j.jobcr.2024.03.002

31. K-H Kim, J-E Kim, S-S Lee, C Lee, M Choi, HS Yong, et al. Developing evidence-based clinical imaging guidelines for the diagnosis of vertically fractured teeth. Oral Radiol. 2024;40:471–83 https://doi.org/10.1007/s11282-024-00766-2

32. GNM Santos, HEC Da Silva, FEL Ossege, PTDS Figueiredo, NDS Melo, CM Stefani, et al. Radiomics in bone pathology of the jaws. Dentomaxillofacial Radiology. 2023;52:20220225 https://doi.org/10.1259/dmfr.20220225

33. SL Tan, KB Patel, and JK Kilgariff. Cemental tears: challenges in the diagnosis and management of an unusual finding associated with rapid localized periodontal and peri-radicular bone loss. Dent Update. 2022;49:895–903 https://doi.org/10.12968/denu.2022.49.11.895

Supplementary Files

This is a list of supplementary files associated with this preprint. Click to download.

- TableS1.xlsx
- TableS2.docx
- FigureS1.tiff